Time Evolution of the Cloud Response to Moisture Intrusions into the Arctic during Winter

YINGHUI LIU

Cooperative Institute for Meteorological Satellite Studies, University of Wisconsin–Madison, Madison, Wisconsin

JEFFREY R. KEY

Center for Satellite Applications and Research, NOAA/NESDIS, Madison, Wisconsin

STEVE VAVRUS

Center for Climatic Research, University of Wisconsin–Madison, Madison, Wisconsin

CIAN WOODS

Department of Meteorology, Stockholm University, Stockholm, Sweden

(Manuscript received 25 December 2017, in final form 12 September 2018)

ABSTRACT

Northward fluxes of moisture and sensible heat into the Arctic affect the atmospheric stability, sea ice and snow cover, clouds, and surface energy budget. Intense moisture fluxes into the Arctic are called moisture intrusions; some can lead to basinwide increases in downward longwave radiation (DLR) at the surface, called downward infrared (IR) events. Using the ERA-Interim reanalysis from 1990 to 2016, this study investigated the time evolution of cloud amount and cloud properties and their impact on the surface radiation fluxes in response to Arctic moisture intrusions and downward IR events during winter for better understanding of the Arctic moisture intrusions. A composite analysis revealed several key features: moisture intrusions produce more clouds and higher cloud liquid and ice water content; positive cloud amount anomalies can persist for over 10 days over the Arctic Ocean during downward IR events; positive high-level and middle-level cloud anomalies are evident in the early stage, and positive low-level cloud anomalies are evident in the late stage. Greater clear-sky DLR and longwave cloud radiative forcing (CRF) over the Arctic Ocean accompany the greater all-sky DLR during the downward IR events. Greater clear-sky DLR can be attributed to higher air temperatures and higher total column water vapor, while greater longwave CRF is the result of larger cloud amount and cloud water content. Longwave CRF anomalies account for approximately 40% of the all-sky DLR anomalies.

1. Introduction

Moisture intrusions are episodes of intense poleward moisture flux into the Arctic. Moisture intrusions are concentrated over the Labrador Sea, North Atlantic, Barents/Kara Sea, and Pacific (Woods et al. 2013). Some of the intrusions can result in greater Arctic basin downward longwave radiation (DLR) for three or more consecutive days, called downward infrared (IR) events (Park et al. 2015). The frequency of the moisture intrusions has been increasing in December and January (Woods and Caballero 2016). Moisture intrusions bring air masses with higher temperatures and moisture to the Arctic, which weakens temperature inversions and lowers the atmospheric stability, increases DLR, and reduces sea ice concentration (Park et al. 2015; Woods and Caballero 2016; Alexeev et al. 2017). Radiation flux anomalies in the wintertime associated with moisture intrusions and cloud amount anomalies likely precondition the sea ice

Denotes content that is immediately available upon publication as open access.

Supplemental information related to this paper is available at the Journals Online website: https://doi.org/10.1175/JCLI-D-17-0896.s1.

Corresponding author: Yinghui Liu, yinghuil@ssec.wisc.edu

DOI: 10.1175/JCLI-D-17-0896.1

TABLE 1. Parameters used in this study from ERA-Interim. Asterisks (*) denote variables derived from variables included in ERA-Interim. [Atmospheric stability = $PT_{850} - PT_{sfc}$, where potential temperature (PT) at 850 hPa is $PT_{850} = T_{850} \times (1000/850)^{0.286}$, and surface potential temperature is $PT_{sfc} = T_{2m} \times (1000/P_{sfc})^{0.286}$.]

Dataset	Parameters	Standard deviation	Spatial domain
ERA-Interim daily	Surface thermal radiation downward (strd)	11.0 W m^{-2}	1° × 1°, 70°–90°N
	Surface thermal radiation net (str)		
	Surface thermal radiation net clear-sky (strc)		
	Surface thermal radiation downward clear-sky (strd − str + strc)*	6.6 W m^{-2}	
	CRF (str − strc)*	5.2 W m^{-2}	
	Cloud amount	4.6%	
	High-, medium- and low-level cloud amount	6.3, 5.5, 5.2%	
	Total column water vapor	0.45 kg m^{-2}	
	Vertical integral of cloud liquid water	3.3 g m^{-2}	
	Vertical integral of cloud frozen water	8.0 g m^{-2}	
	Air temperature at 850 hPa T_{850}	2.0 K	
	2-m air temperature T_{2m}	2.0 K	
	Surface atmosphere pressure P_{sfc}		
	Atmosphere stability*	1.5 K	
	Vertical integral of divergence of moisture flux	9.7 kg m^{-2} s^{-1}	
Terra MODIS daily	Cloud amount	9.0%	1° × 1°, 70°–90°N
CloudSat 2B-GEOPROF	Total and high-, medium-, and low-level cloud amount	4.7, 3.6, 4.6, 4.0%	70°–82.5°N
CloudSat 2B-CWC-RO	Cloud ice water content	2.3 g m^{-2}	70°–82.5°N

thickness for the sea ice concentration changes in the following summer (Johansson et al. 2017; Letterly et al. 2016; Park et al. 2015; Liu and Key 2014).

Johansson et al. (2017) showed the impact of moisture intrusions on cloud amount and cloud radiative heating in all four seasons. Moisture intrusions lead to a mean surface warming of up to 5.3 K (±3.3 K) in winter and 2.3 K (±1.6 K) in summer over the Arctic Ocean and a cloud radiative heating of up to 0.15 K day^{-1} through an increase in cloud amount up to 30%. However, a detailed time evolution of cloud amount and cloud properties and their impact on surface radiation fluxes during moisture intrusions was not provided in previous studies. For a better understanding of the impact of moisture intrusions in the Arctic, we conducted this process-oriented study to provide the time evolution of surface radiation fluxes, cloud amount, cloud properties, and other variables during moisture intrusions into the Arctic and downward IR events. Because of the interest in wintertime preconditioning of these moisture intrusions for changes in sea ice characteristics the following summer, we focused on the winter season, from November to March.

2. Data and methods

a. Data

Daily ECMWF interim reanalysis (ERA-Interim) variables at the surface and at multiple pressure levels, with a spatial resolution of 1.0° × 1.0° from 1990 to 2016, were used (Dee et al. 2011). Only data after 1990 were included to emphasize the stronger polar amplification signal that occurred after 1990 (Woods and Caballero 2016). Woods and Caballero (2016) also suggested that the post-1990 ERA-Interim reanalysis tends to have higher observational consistency. Variables used in this study are listed in Table 1. Because of the differences in the formation, maintenance, and dissipation process of high-, middle-, and low-level clouds in the Arctic and the complex process determining the Arctic cloud phases (Curry et al. 1996), high-level cloud, middle-level cloud, low-level cloud, total clouds, cloud ice water content, and cloud liquid water content were included. The high-level cloud in ERA-Interim is cloud with the ratio of the pressure of the cloud layer to surface pressure between 0.0 and 0.45; middle- and low-level cloud are between 0.45 and 0.8 and between 0.8 and 1.0, respectively. Large uncertainties and inconsistencies exist in reanalysis cloud amount and surface radiation fluxes, especially in winter at high latitudes (Zib et al. 2012; Walsh et al. 2009; Zygmuntowska et al. 2012; Liu and Key 2016; Liu and Schweiger 2017), and thus we used cloud products from satellite imagers (e.g., MODIS) and from satellite-borne active sensors [e.g., cloud profiling radar (CPR)] onboard *CloudSat* to verify some of the results based on reanalysis.

Level-3 monthly global products from the MODIS instrument on the NASA *Terra* satellite, at 1° latitude × 1° longitude over the period 2000–16, were used. The

MODIS level-3 daily cloud statistics are calculated from all level-2 MODIS cloud mask granules with an equal-angle 1° latitude × 1° longitude grid, with cloud fraction as the percentage of cloudy and uncertain and/or probably cloudy level-2 pixels. MODIS provides a robust cloud mask product in the polar regions with improvements in the cloud detection algorithm over recent years, but it remains challenging to detect polar night clouds using satellite imagers (Ackerman et al. 1998; Liu et al. 2004; Frey et al. 2008). Validation with active satellite sensor cloud products shows overall agreement, with some dependence of MODIS cloud amount on sea ice concentration (Liu et al. 2010).

Observations from CPR onboard *CloudSat* can penetrate deep within almost all nonprecipitating clouds (Stephens et al. 2002) and thus can provide a complete cloud vertical distribution. *CloudSat* has limitations in detecting thin cirrus, especially with small particle sizes, and has surface contamination up to a height of about 0.96 km, where weaker cloud signals are missed (Liu et al. 2017). A level-2 geometrical profiling product (2B-GEOPROF) provides a CPR echo mask at 125 vertical range bins, with a bin size of 240 m (Marchand et al. 2008). A threshold of 20 was applied to 2B-GEOPROF cloud mask profiles to generate a cloud mask including clouds with weak echo, good echo, and strong echo with values larger than 20, while clouds with very weak echo and echo with likely surface clutter were excluded (Mace et al. 2009). The 2B-GEOPROF products from 2006 to 2016 were used.

A level-2 *CloudSat* product, the *CloudSat* radar-only cloud water content product (2B-CWC-RO), estimates cloud liquid and ice water content (Austin et al. 2009). This product retrieves water content and effective radius with the assumption that the radar profile is due to a single water phase, either liquid or ice. With collocated ECMWF temperature profiles, this product combines separate liquid and ice profiles into a mixture of ice and liquid phases within the proper temperature range. Only retrievals of ice water content were used for its better retrieval quality than that of liquid water content. The 2B-CWC-RO products from 2006 to 2016 were used.

b. Methods

Woods et al. (2013) defined a moisture intrusion as a vertically integrated poleward moisture flux across 70°N larger than 200 Tg per day per degree of longitude for at least 1.5 consecutive days at every point within a sector of at least 9° zonal extent. They also rejected those moisture intrusions that do not penetrate sufficiently deep into the Arctic by computing forward Lagrangian trajectories from each of the grid points in an event for 6 days and retaining only those events with at least 40% of the trajectories across 80°N. Johansson et al. (2017) defined ''water vapor intrusions'' into the Arctic as the vertically integrated poleward moisture flux across 70°N exceeding the 90th percentile for at least 24 h in each season. Woods et al. (2013) and Johansson et al. (2017) focused on four geographic sectors of the major pathways of Arctic moisture intrusions: the Atlantic (30°W–25°E), the Barents/Kara Seas (25°–90°E), the Pacific (145°E–130°W), and the Labrador Sea (90°–30°W). In this study, we applied a stricter definition of moisture intrusion in each sector as an event that meets the criteria of both definitions from Woods et al. (2013) and Johansson et al. (2017). The winter is defined here as from November to March. Using ERA-Interim data from 1990 to 2016, we identified 68, 54, 59, and 36 events for the Atlantic, Barents/Kara, Pacific, and Labrador sectors, respectively. In section 3a we focus on these events.

Park et al. (2015) defined a downward IR event based on DLR data from ERA-Interim. A downward IR event was defined as in Park et al. (2015): a time period with the Arctic-mean DLR larger than one standard deviation for three or more consecutive days, with the beginning of an event not within seven days of any other events. The seasonal cycle of the daily average of the DLR in ERA-Interim was defined as a 30-day moving average of the 27-yr mean (1990–2016), and the seasonal cycle was then removed from each grid cell. DLR after seasonal cycle removal was averaged from 70° to 90°N with weights of the cosine of the latitude, and then detrended to create a time series of daily Arctic-mean DLR to calculate the standard deviation and to identify the downward IR events (Park et al. 2015). Correlation analysis showed that the poleward moisture flux is associated with these IR events, and lag correlation illustrates that anomalously higher averaged poleward moisture flux between 70° and 75°N leads these IR events from 1 to 3 days (Park et al. 2015). In this study, we identify 50 winter IR events occurring between 1 November and the following 31 March from 1990 to 2016 using ERA-Interim. Of the 50 IR events, 25 events have their first days within 1–5 days from the start of a moisture intrusion through the Atlantic sector, and 16, 4, and 3 respectively, through the Barents/Kara, Pacific, and Labrador sectors, with a mean lead time of 3 days. Two IR events were not associated with moisture intrusions. In section 3b we focus on these 50 events, a subset of all moisture intrusions that have a basinwide impact on the surface DLR.

Composite analyses of the following variables were performed: all-sky DLR, clear-sky DLR, longwave cloud radiative forcing (CRF), cloud amount, air temperature at 2 m and 850 hPa, total column water vapor, cloud ice water content, cloud liquid water content, low

troposphere stability, geopotential height at 850 and 500 hPa from ERA-Interim, total cloud amount from MODIS, cloud amount from 2B-GEOPROF, and cloud water content from 2B-CWC-RO. Daily total cloud amount (including at high, middle, and low levels) and cloud water content in the Arctic from *CloudSat* 2B-GEOPROF and 2B-CWC-RO were derived using methods detailed in Liu et al. (2012a). After removal of their seasonal means, defined as a 30-day moving average of the 27-yr mean (1990–2016) (2006–16 for cloud amount from 2B-GEOPROF and cloud water content from 2B-CWC-RO), all these variables were detrended and composited from lag day −5 to lag day 14 as the mean for all the moisture intrusions in each of those four sectors and also for all the IR events. After the removal of the seasonal mean, each variable was averaged from 70° to 90°N with weights of the cosine of the latitude, detrended, and its standard deviation was calculated (Table 1). These standard deviations were used to normalize the averaged basinwide anomalies, and normalized anomalies were shown in some of the figures.

A Student's *t* test was used to estimate the significance level of the composite results. In the figures of area-averaged standardized anomalies, composites different from 0 with over 95% confidence level were shown. In the figures of anomalies at every grid location, composites different from 0 with over 90% confidence level were shown. This lower confidence level was used due to noisier grid-level data than area averages.

3. Results

a. Composite analysis during moisture intrusions

The time evolution of variables during the moisture intrusions in the four sectors share similar features. We illustrate the time evolution of variables during the moisture intrusions in the Barents/Kara sector in detail. We also present the detailed time evolution during the moisture intrusions of other three sectors, with figures shown in the online supplemental material.

During the moisture intrusions in the Barents/Kara sector, all-sky DLR starts to show anomalies of more than $8\,W\,m^{-2}$ over northern Europe, the Barents Sea, and the Kara Sea at the beginning. These anomalies increase and reach a maximum of over $20\,W\,m^{-2}$ at lag day 6 and extend to the Laptev Sea and north-central Russia. The anomalies begin to decrease in magnitude after lag day 6 and are less in spatial extent. The anomalies remain over $5\,W\,m^{-2}$ at lag day 12, except over northern Europe (Fig. 1). The time evolution of temperature at 850 hPa (Fig. 1) and at other levels (not shown) and the total column water vapor (Fig. 1) share similar features with the time evolution of DLR. The time evolution of 2-m air temperature also shares similar features, except that the positive anomalies after lag day 6 decrease more slowly due to the higher heat capacity of the land and thus longer memory. Geopotential height anomalies at 500 hPa (Fig. 1) and at other levels (not shown) show positive anomalies over north-central Russia and negative anomalies over the Greenland–Iceland–Norwegian (GIN) Seas, which aids moisture advection into the Arctic through the Barents and Kara Seas. This spatial pattern remains unchanged during the moisture intrusions, with the maximum magnitude at lag day 3.

Anomalies in all-sky DLR come from the anomalies in both clear-sky DLR and longwave CRF. Changes in temperature and moisture at all vertical levels contribute to the clear-sky DLR; thus, the time evolution of clear-sky DLR shares similar features with those of temperature at 850 hPa and of total column water vapor (Fig. 2). Time evolutions of longwave CRF have positive anomalies over north-central Russia, the Kara Sea, and the North Pole from lag day 0 to lag day 12, with the maximum from lag day 3 to lag day 6. Longwave CRF is determined mainly by cloud macrophysical and microphysical properties, including cloud amount and cloud water content. Time evolutions of total cloud amount and cloud ice water content anomalies share similar features, with positive anomalies over north-central Russia, the Kara Sea, and the North Pole from lag day 0 to lag day 9. Total cloud amount anomalies remain unchanged throughout to lag day 12 and may expand to larger spatial area after lag day 3. Cloud ice water content anomalies have a positive maximum at lag day 3 and remain positive until lag day 9 (Fig. 2). Time evolutions of low-level cloud have the same features as those of total cloud amount, while the high-level cloud have maximum positive anomalies over the Barents and Kara Seas at lag day 3. This positive anomaly remains until lag day 6 (Fig. 3). The anomalies in low-level clouds are more persistent and cover a larger area than those of high-level and middle-level clouds.

All the anomalies from the moisture intrusions in the Barents/Kara sector are limited to the Atlantic side of the Arctic Ocean. The anomalies averaged over the area between 70° and 90°N latitude and between 60° and 150°E are shown for all-sky DLR, clear-sky DLR, longwave CRF, temperatures at 850 hPa and 2 m, total column water vapor, and cloud ice and liquid water content (Fig. 4). These averaged anomalies are greater than those averaged over the entire Arctic Ocean between 70° and 90°N latitude (see Fig. S1 in the online supplemental material). Most of the composite values are significant at the 95% confidence level after the start

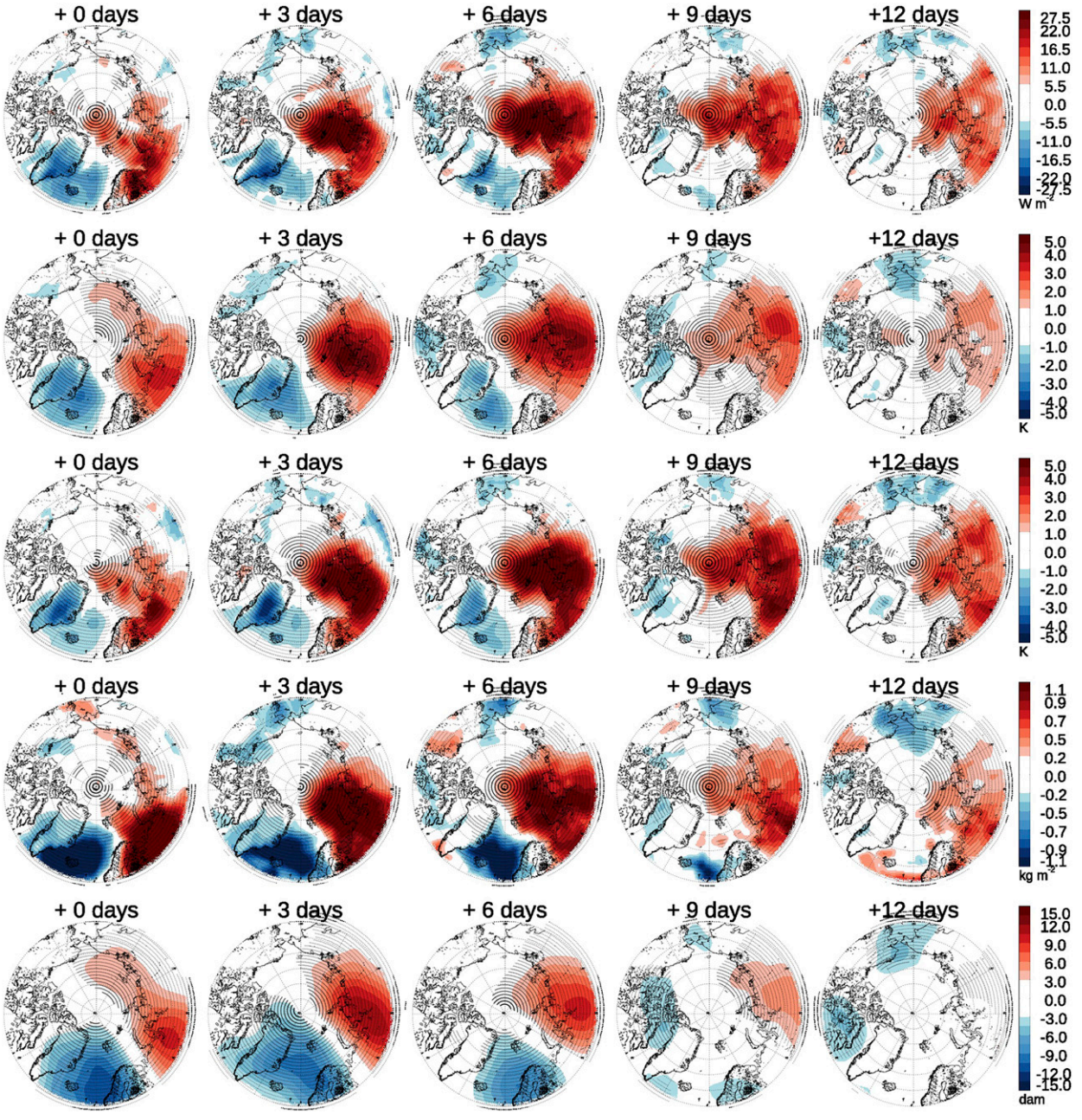

FIG. 1. Composite of the time evolution of anomalies in (first row) all-sky downward longwave radiation, (second row) temperature at 850 hPa, (third row) 2-m air temperature, (fourth row) total column water vapor, and (fifth row) 500-hPa geopotential height during moisture intrusions in the Barents/Kara sector. Composite values with a significance level higher than 90% are labeled with a black plus sign.

of the moisture intrusions except atmospheric stability from lag day 0 to lag day 6, moisture convergence after lag day 4, and cloud liquid water content and high-level cloud after lag day 4. The longwave CRF accounts for 34.3%–41.3% of the all-sky DLR from lag day 0 to lag day 10 averaged over the area between 70° and 90°N and between 60° and 150°E.

Time evolutions of anomalies of all variables during the moisture intrusions in the Atlantic sector share similar features to those in the Barents/Kara sector (Figs. S2–S6). All the anomalies are limited to the Atlantic side of the Arctic; their averages over the area between 70° and 90°N latitude, and between 30° and 120°E are greater than the averages over the entire

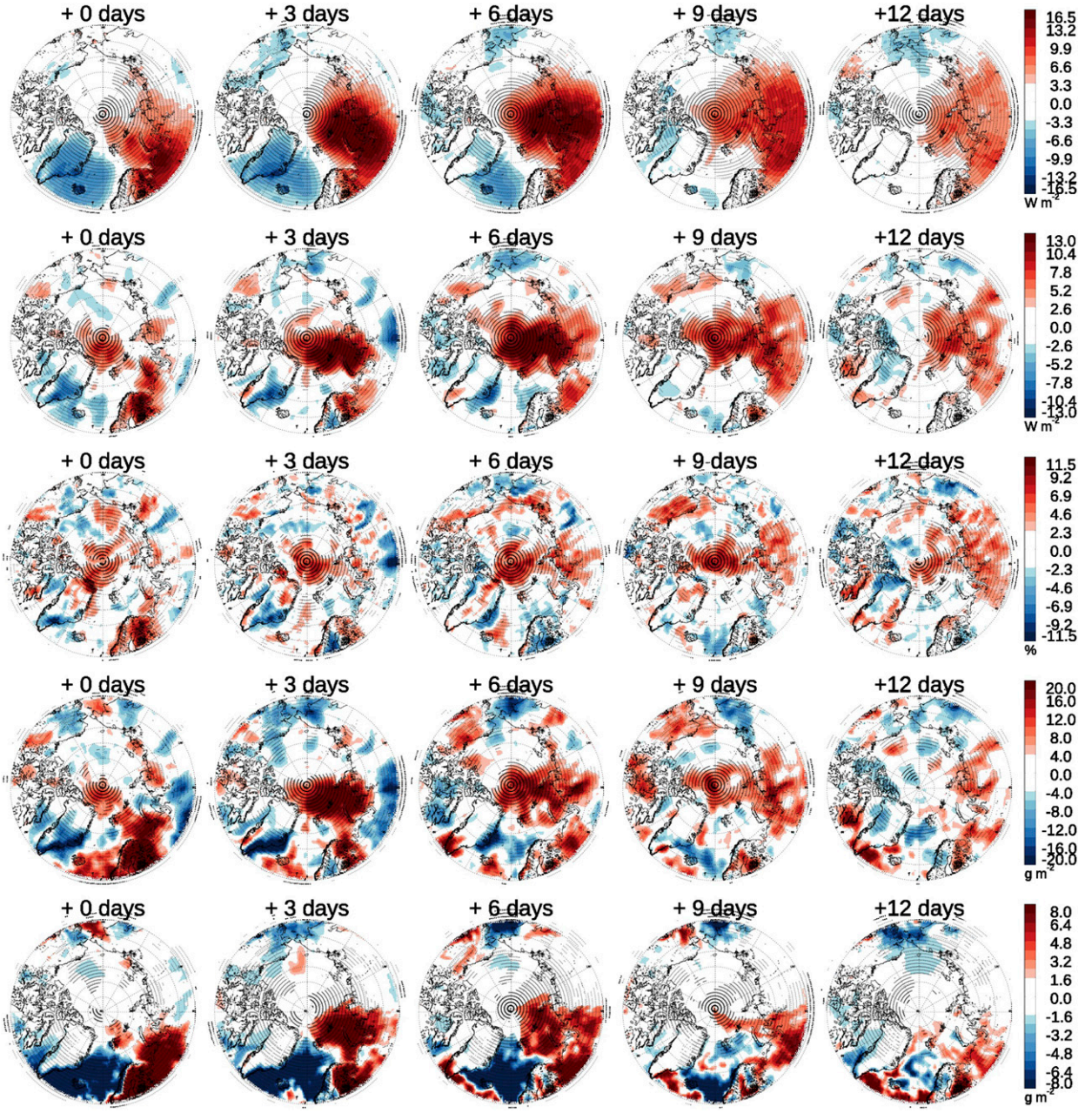

FIG. 2. Composite of the time evolution of anomalies in (first row) clear-sky downward longwave radiation, (second row) longwave cloud forcing, (third row) total cloud amount, (fourth row) cloud ice water content, and (fifth row) cloud liquid water content during moisture intrusions over the Barents/Kara sector. Composite values with a significance level higher than 90% are labeled with a black plus sign.

Arctic Ocean. Different features compared to those for the Barents/Kara sector include the following: 1) all the positive anomalies appear over the GIN Seas, Nansen Basin, and Barents Sea; 2) geopotential heights have positive anomalies over northern Europe and the Barents Sea and negative anomalies from Greenland to the Canada Archipelago, and remain in this pattern during moisture intrusions; and 3) the longwave CRF accounts for 17.0%–34.0% of the all-sky DLR from lag day 0 to lag day 10, averaged over the area 70°–90°N, 30°–120°E.

Time evolutions of anomalies of all variables during the moisture intrusions in the Pacific sector share similar features, shown in Figs. S7–S11, as those in the Barents/Kara sector. All the anomalies are limited to the Pacific side of the Arctic—their averages over the area 70°–90°N,

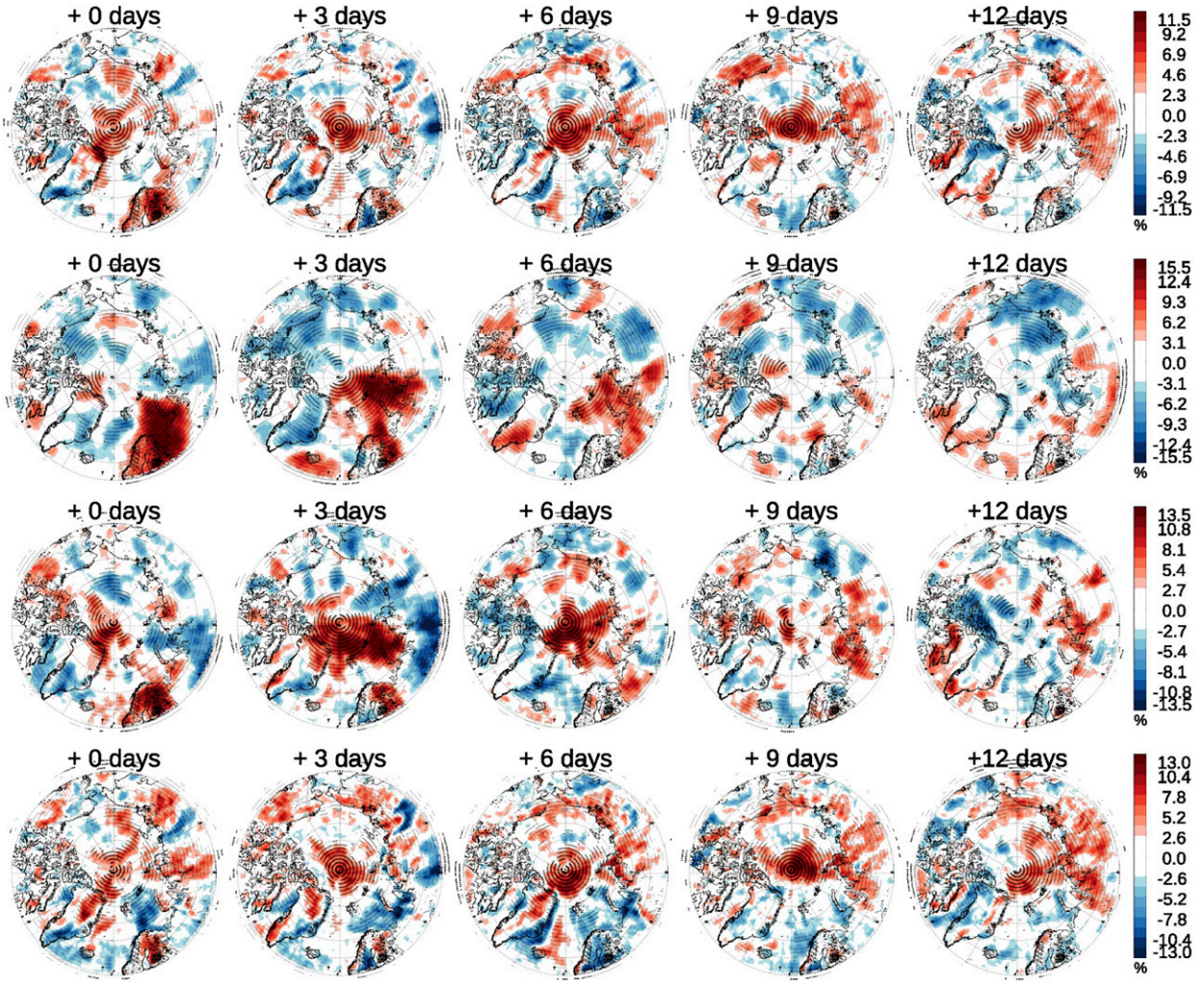

FIG. 3. Composite of the time evolution of anomalies in (first row) total cloud amount, (second row) high-level cloud amount, (third row) middle-level cloud amount, and (fourth row) low-level cloud amount during moisture intrusions over the Barents/Kara Sea sector. Composite values with a significance level higher than 90% are labeled with a black plus sign.

150°E–120°W are greater than the averages over the entire Arctic Ocean. Different features compared to those for the Barents/Kara sector include that 1) all the positive anomalies appear over the Pacific side of the Arctic Ocean, Alaska, and northeastern Russia; 2) geopotential heights have positive anomalies over Alaska and the Beaufort Sea and negative anomalies over north-central Russia, and remain in this pattern during moisture intrusions; 3) all anomalies disappear after lag day 9, except that positive low-level cloud amount anomalies remain at lag day 12; and 4) the longwave CRF accounts for 12.3%–36.2% of the all-sky DLR from lag day 0 to lag day 9, averaged over the area 70°–90°N, 150°E–120°W.

Time evolutions of anomalies of all variables during the moisture intrusions in the Labrador sector share similar features (not shown) as those of the Barents/Kara sector. All the anomalies are limited to Greenland, Baffin Bay, and part of the Canadian Archipelago Seas adjacent to Baffin Bay. Geopotential heights have positive anomalies centered over the southern part of the Greenland, and negative anomalies over the Beaufort Sea.

b. Composite analysis during downward IR events

On average, the 50 downward IR events described above were led by moisture intrusions by 3 days. Therefore, the lag day −3 (and similarly 0, 3, 6, 9, 12, etc.) of an IR event can be compared to the lag day 0 (3, 6, 9, 12, 15, etc., respectively) of a moisture intrusion.

1) LONGWAVE RADIATION

The time evolutions of all-sky DLR, clear-sky DLR, and longwave CRF during IR events are shown in Fig. 5.

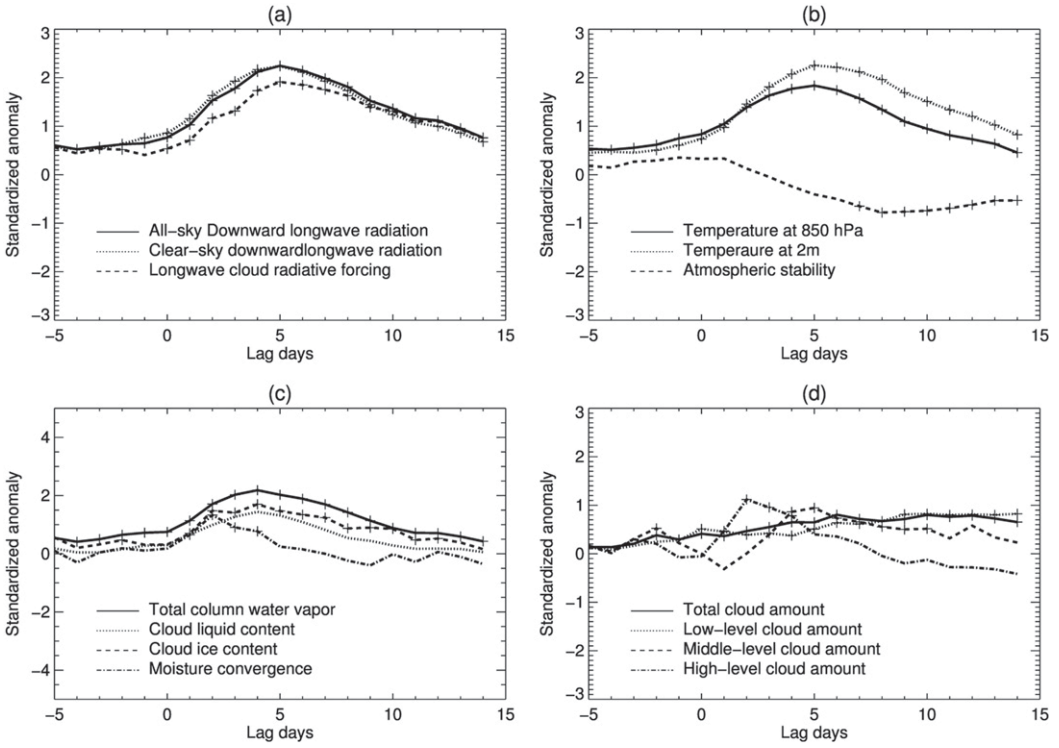

FIG. 4. Time evolution of standardized anomalies in (a) all-sky downward longwave radiation, clear-sky downward longwave radiation, and longwave radiation cloud forcing; (b) air temperature at 2 m, air temperature at 850 hPa, and lower-level atmospheric stability; (c) total column water vapor, cloud liquid water content, cloud ice water content, and moisture convergence; and (d) total cloud amount and low-, medium-, and high-level cloud amount averaged over 70°–90°N, 60°–150°E during moisture intrusions over the Barents/Kara Sea sector. Composite values with a significance level higher than 95% are labeled with a plus sign.

All-sky DLR has positive anomalies over the Nansen Basin and the Kara Sea and negative anomalies over the Canadian Archipelago before lag day 0. From lag day 0 to lag day 6, positive DLR anomalies are over most of the Arctic Ocean and northeastern Russia; negative DLR anomalies are over the Canadian Archipelago. Positive all-sky DLR anomalies are larger than two standard deviations over the Nansen Basin and the Kara Sea, extending gradually to the North Pole, and farther to the central Arctic and the Chukchi Sea. From lag day 6 to lag day 9, DLR positive anomalies remain over most of the Arctic Ocean. Spatial patterns and the evolution of the clear-sky DLR and longwave CRF anomalies mimic those of the all-sky DLR. One difference is that a positive longwave CRF anomaly higher than two standard deviations shifts northward more to the central Arctic Ocean compared to all-sky DLR between lag day 0 and lag day 6. Of the total positive all-sky DLR anomalies, the proportions of the clear-sky DLR anomaly and the longwave CRF anomaly are comparable, with approximately 60% from the clear-sky DLR anomaly and 40% from the longwave CRF anomaly. The spatial distribution of the ratio of longwave CRF to all-sky DLR shows relatively higher longwave CRF contributions over regions north to the Canadian Archipelago.

Averaged anomalies between 70° and 90°N are larger than one standard deviation from lag day 0 to lag day 8 for all-sky DLR, clear-sky DLR, and longwave CRF and remain larger than 0.5 standard deviation from lag day 9 to lag day 11 (Fig. 6a). The standard deviations for all-sky DLR, clear-sky DLR, and longwave CRF are 11.0, 6.6, and 5.2 $W m^{-2}$, respectively. The normalized anomalies follow each other rather closely, which shows that the averaged longwave CRF is comparable to averaged clear-sky DLR, and accounts for approximately 40% of averaged all-sky DLR, which is consistent with the spatial patterns shown in Fig. 5.

2) CLEAR-SKY DLR AND ITS RELATED VARIABLES

Positive clear-sky DLR anomalies are spatially associated with a higher air temperature at each atmospheric layer and larger integrated column water vapor during

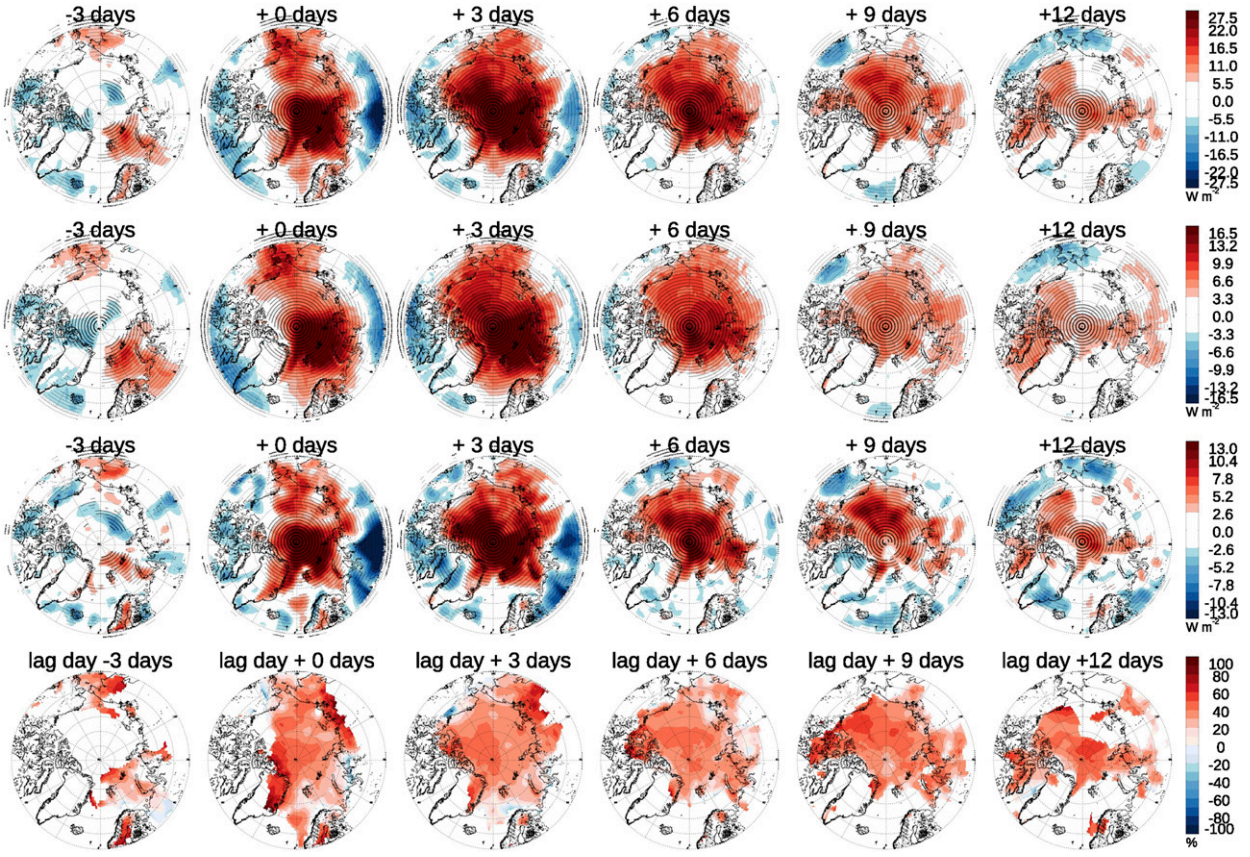

FIG. 5. Composites of the time evolution of anomalies in (first row) all-sky downward longwave radiation, (second row) clear-sky downward longwave radiation, (third row) longwave cloud forcing, and (fourth row) the ratio of longwave cloud forcing to all-sky downward longwave radiation during downward IR events. Composite values with a significance level higher than 90% are labeled with a black plus sign.

IR events (Fig. 7). The air temperature at 850 hPa shows positive anomalies over the Nansen Basin and the Kara Sea 3 days before the onset of IR events. Positive air temperature anomalies at 850 hPa appear over most of the Arctic Ocean from lag day 0 to lag day 9, with higher positive anomalies over the Kara Sea and the North Pole from lag day 0 to lag day 3, and weaker positive anomalies after lag day 9. The spatial pattern and evolution of total column water vapor anomaly resemble that of the air temperature anomaly at 850 hPa, except that high positive water vapor anomalies occur over the GIN Seas and the Barents Sea from lag day 0 to lag day 3.

Averaged anomalies of clear-sky DLR between 70° and 90°N show similar evolutions as air temperature at 2 m and at 850 hPa, and total column water vapor (Figs. 6b,c). Air temperature at 2 m has positive anomalies above one standard deviation from lag day 0 to lag day 9 and remains above a 0.5 standard deviation until lag day 14. Air temperature at 850 hPa has positive anomalies of more than one standard deviation from lag day 0 to lag day 6 and remains higher than 0.5 standard deviation until lag day 9. Total column water vapor has positive anomalies higher than one standard deviation from lag day 0 to lag day 7 and remains higher than 0.5 standard deviation until lag day 10 (Fig. 6c). Air temperature increases at the lower layer (e.g., at 2 m) last longer than those at higher layers (e.g., 850 hPa), which might be due to the higher heat capacity of surface and thus longer memory. More open water due to sea ice melting following the anomalously greater DLR may warm the lower atmosphere even more than higher layers (Park et al. 2015). Both temperature anomaly and total column water vapor anomaly evolutions resemble that of clear-sky DLR with both correlations higher than 0.95 with a 95% confidence level, which suggests a contribution of moisture flux and heat flux to the clear-sky DLR anomalies.

Anomalies in large-scale circulation favor the moisture and heat advection from lower latitudes northward into the Arctic (Fig. 8). Starting at lag day −3, a pattern with positive geopotential height anomalies at 850 and 500 hPa over northern Europe and negative geopotential

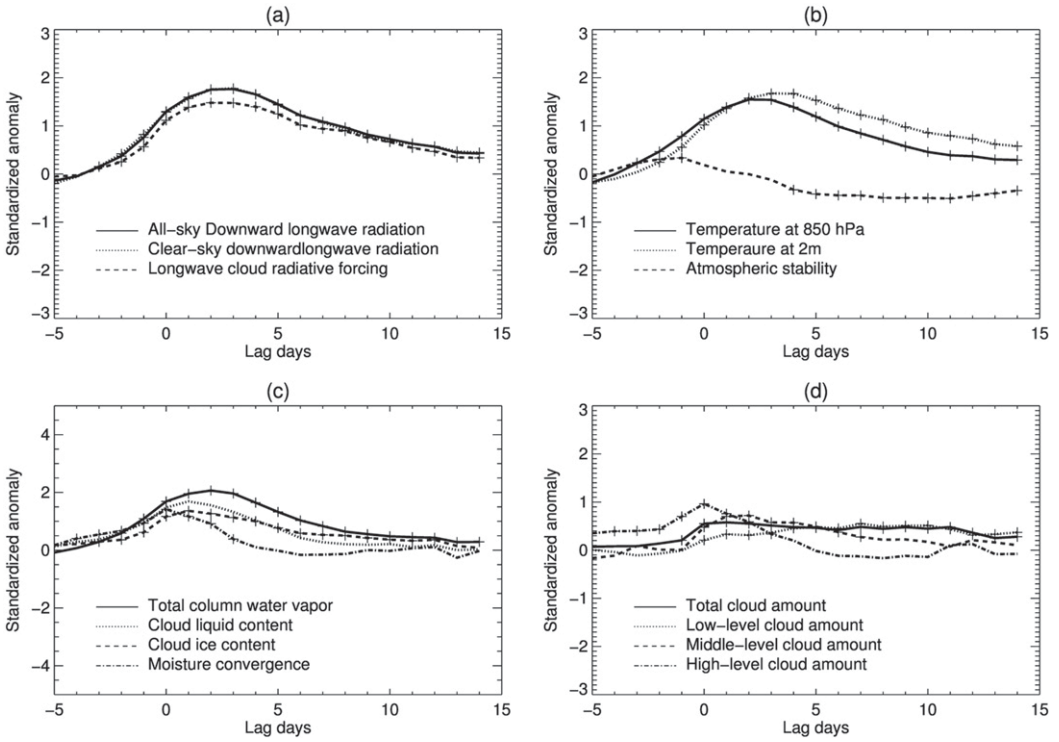

FIG. 6. Time evolution of standardized anomalies in (a) all-sky downward longwave radiation, clear-sky downward longwave radiation, and longwave radiation cloud forcing; (b) air temperature at 2 m, air temperature at 850 hPa, and lower-level atmospheric stability; (c) total column water vapor, cloud liquid water content, cloud ice water content, and moisture convergence; and (d) total cloud amount and low-, middle-, and high-level cloud amount during downward IR events averaged over the area between 70° and 90°N standardized by their standard deviations. Composite values with a significance level higher than 95% are labeled with a plus sign.

height anomalies over the GIN Seas, Greenland, and Baffin Bay appears; from lag day −3 to lag day 3, this pattern strengthens, and the center of the positive geopotential height anomaly moves to north-central Russia, and the center of the negative geopotential height anomaly moves toward to the Canada Archipelago Seas; after lag day 3, the strength of the pattern starts to weaken, with the center of the positive (negative) geopotential height anomaly continuing to move toward northeastern Russia (Alaska region). Compared to the unchanged large-scale atmospheric pattern in the composite analysis of moisture intrusions in the four sectors in section 3a, this time-evolving large-scale pattern helps the heat and moisture move from the lower latitudes to the Atlantic side of the Arctic Ocean, farther into the central Arctic Ocean and the Pacific side of the Arctic Ocean.

3) LONGWAVE CRF AND ITS RELATED VARIABLES

Positive longwave CRF anomalies over most of the Arctic Ocean during IR events might be attributed to the greater cloud amount, higher cloud ice water content, and higher cloud liquid water content in the early stage over the Atlantic side of the Arctic Ocean (Fig. 9). Cloud amount shows generally positive anomalies over a large area of the Arctic Ocean, the Canada Archipelago Seas, and northeastern Russia from lag day 0 to lag day 9. The positive cloud amount anomalies are higher north of the Canada Archipelago. Cloud ice water content shows generally positive anomalies over the Arctic Ocean from lag day 0 to lag day 9. Similar to that of cloud amount, positive anomalies of cloud ice water content are larger over the central part of the Arctic Ocean. Maximum anomalies of both cloud amount and cloud ice water content appear to extend from the Nansen Basin and the Kara Sea northward to the central Arctic. Cloud liquid water content shows high positive anomalies over the GIN Seas, the Nansen Basin, and the Kara Sea from lag day 0 to lag day 3, and these appear to extend northward to the central part of the Arctic Ocean from lag day 0 to lag day 3. Positive anomalies of cloud liquid water content over most of the central part of the Arctic Ocean are less than a half

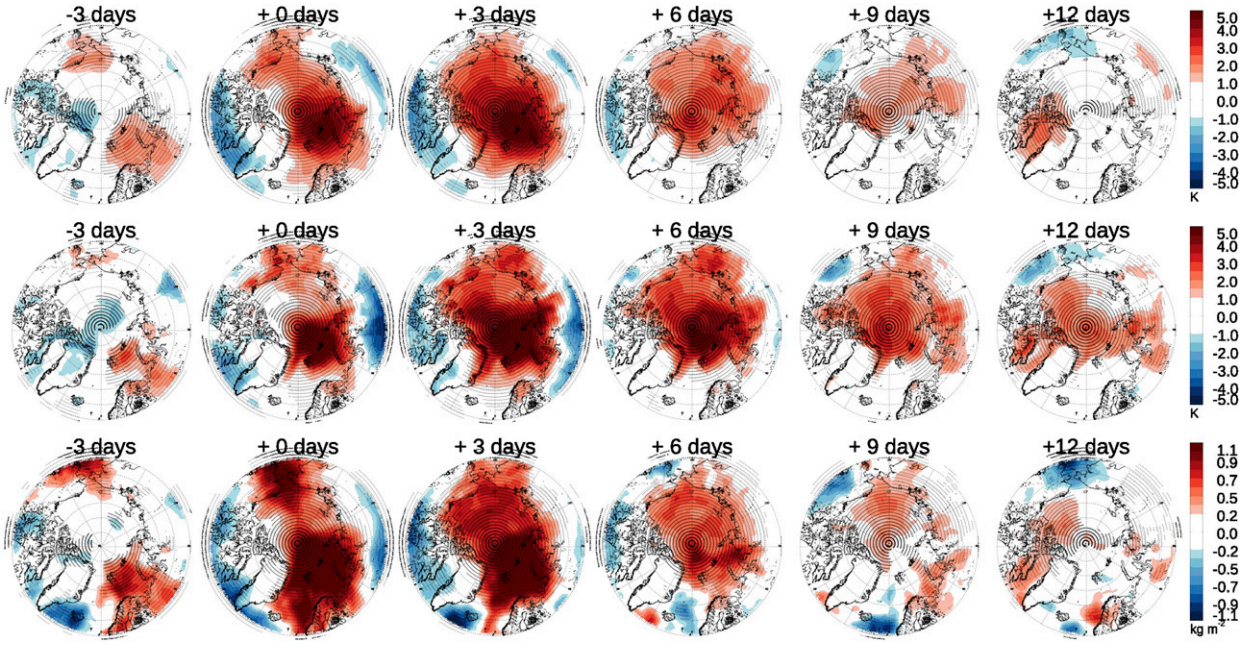

FIG. 7. Composites of the time evolution of anomalies in air temperature at (top) 850 hPa and (middle) 2 m and (bottom) integrated column water vapor during downward IR events. Composite values with a significance level higher than 90% are labeled with a black plus sign.

standard deviation, as are the anomalies after lag day 3 over most of the Arctic Ocean.

Averaged anomalies over the area between 70° and 90°N show different evolutions of total cloud amount, cloud ice water content, and cloud liquid water content (Figs. 6c,d). Total cloud amount has positive anomalies higher than 0.5 standard deviation and lower than one standard deviation from lag day 0 to lag day 10; cloud ice water content has positive anomalies higher than one standard deviation from lag day 0 to lag day 4, and these anomalies remain higher than 0.5 standard deviation until lag day 9 (Fig. 6c); cloud liquid water content has positive anomalies higher than one standard deviation from lag day 0 to lag day 4, and quickly decreases to lower than 0.5 standard deviation at lag day 6. The confidence level of the cloud liquid water anomalies is lower than 95%. Features of these evolutions are consistent with spatial patterns shown in Fig. 9, with positive anomalies of total cloud amount over a relatively limited area and with positive anomalies of cloud liquid water content in the early stage of the IR events. The correlations between total cloud amount, cloud ice water

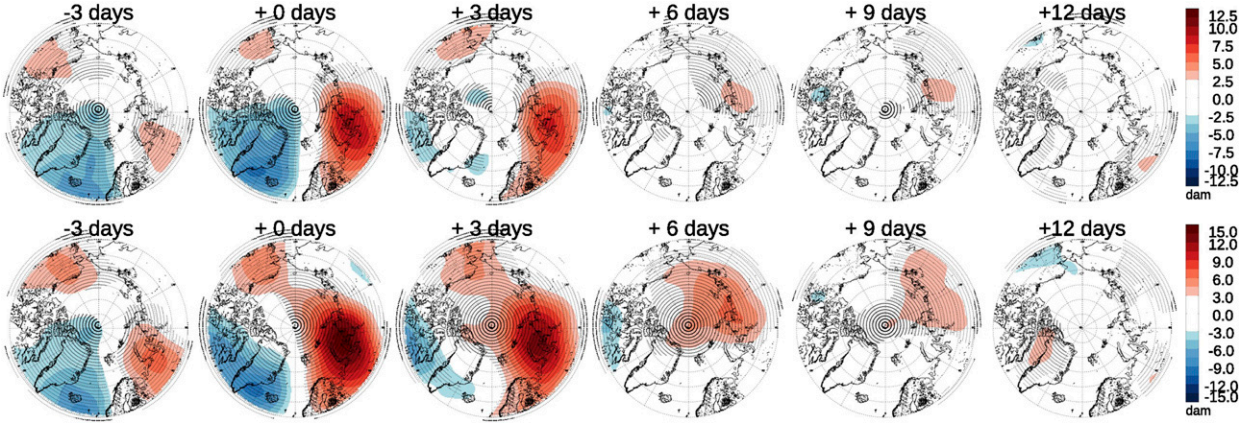

FIG. 8. Composite of the time evolution of anomalies in geopotential height at (top) 850 and (bottom) 500 hPa during downward IR events. Composite values with a significance level higher than 90% are labeled with a black plus sign.

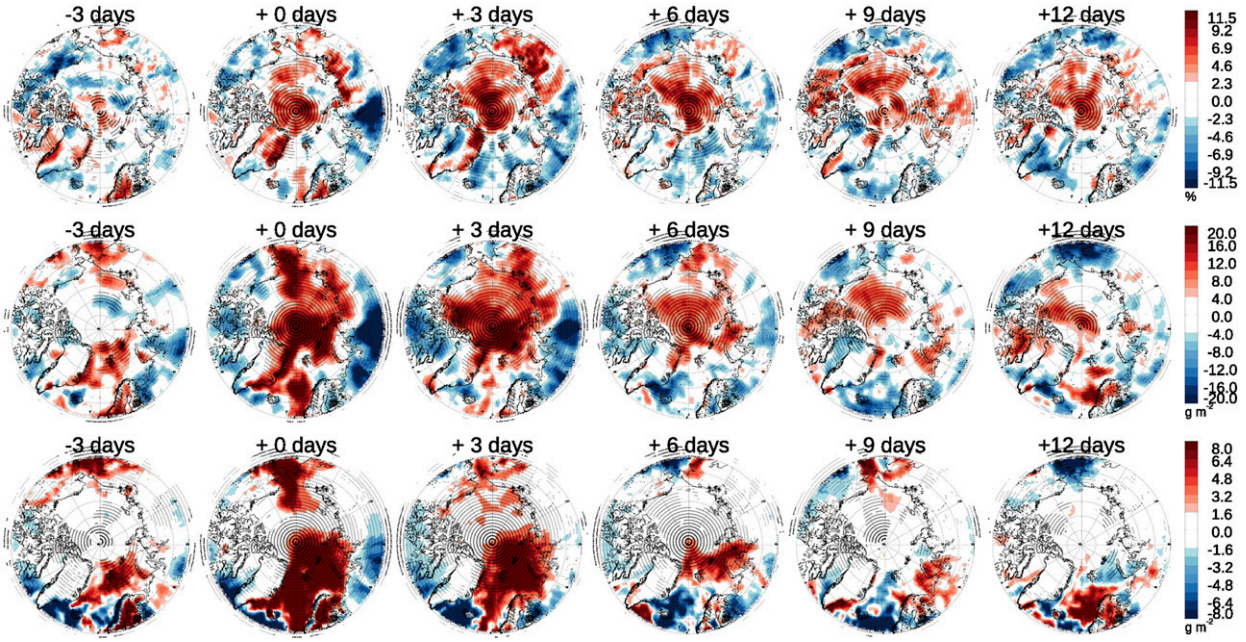

FIG. 9. Composite of the time evolution of anomalies in (top) total cloud amount, (middle) cloud ice water content, and (bottom) cloud liquid water content during downward IR events. Composite values with a significance level higher than 90% are labeled with a black plus sign.

content, cloud liquid water content, and longwave CRF are 0.93, 0.94, and 0.76, respectively (significance level 95%), which indicates that the anomalies in the longwave CRF might originate more from the changes in the cloud amount and cloud ice water content than from the changes in cloud liquid water content in the ERA-Interim. It should be noted that the averaged moisture convergence anomalies are larger than one standard deviation in lag day 0 and lag day 1 and then quickly diminish to be less than 0.5 standard deviation at day 4. The significance level of the moisture convergence anomalies is less than 95% after lag day 3. This illuminates a strong pulse of the moisture convergence at the beginning of the IR events, followed by a quick dissipation in the moisture convergence. This quick transition is consistent with the findings in Park et al. (2015).

Decomposing the cloud evolution by level helps to explain the physical processes involved in the moisture intrusion and IR events. The evolution of low-, middle-, and high-level cloud amount during the IR events shows similarities and differences (Fig. 10). Both low-level and middle-level clouds have generally negative anomalies over land except in northeastern Russia. Positive anomalies of low- and middle-level cloud amount have similar spatial distributions from lag day −3 to lag day 6, with positive anomalies of both low- and middle-level cloud amount mainly over the central part of the Arctic Ocean. After lag day 6, the positive anomaly of low-level cloud amount remains over the central part of the Arctic Ocean and seems to extend spatially, while the positive anomaly of middle-level cloud starts to diminish. High-level cloud shows positive anomalies over the GIN Seas, the Barents Sea, and the Kara Sea from lag day −3 to lag day 0, and these positive anomalies start to diminish afterward. The spatial patterns of the low-level cloud anomalies resemble those of the total cloud anomalies the most, with less resemblance of the middle-level cloud anomalies with total cloud anomalies.

None of averaged anomalies over the area between 70° and 90°N of the low-, middle-, and high-level cloud is higher than one standard deviation, as is the case for total cloud (Fig. 6d). High-level cloud shows relative higher positive anomalies from lag day 0 to lag day 2, and quickly decreases to be less than 0.5 standard deviation, reflecting the higher positive anomalies over the GIN Seas, the Barents Sea, and the Kara Sea in the early stage and subsequent quick diminishing. Middle-level cloud anomaly shows a similar evolution to the total cloud from lag day 0 to lag day 4 and then slowly decreases to be less than 0.5 standard deviation afterward. Significance levels of the high-level cloud anomalies after lag day 3 and of middle-level cloud anomalies after lag day 7 are less than 95%. Low-level cloud shows relatively smaller positive anomalies than the middle-level and the total cloud from lag day 0 to lag day 4 and then follows closely the total cloud anomaly until lag day

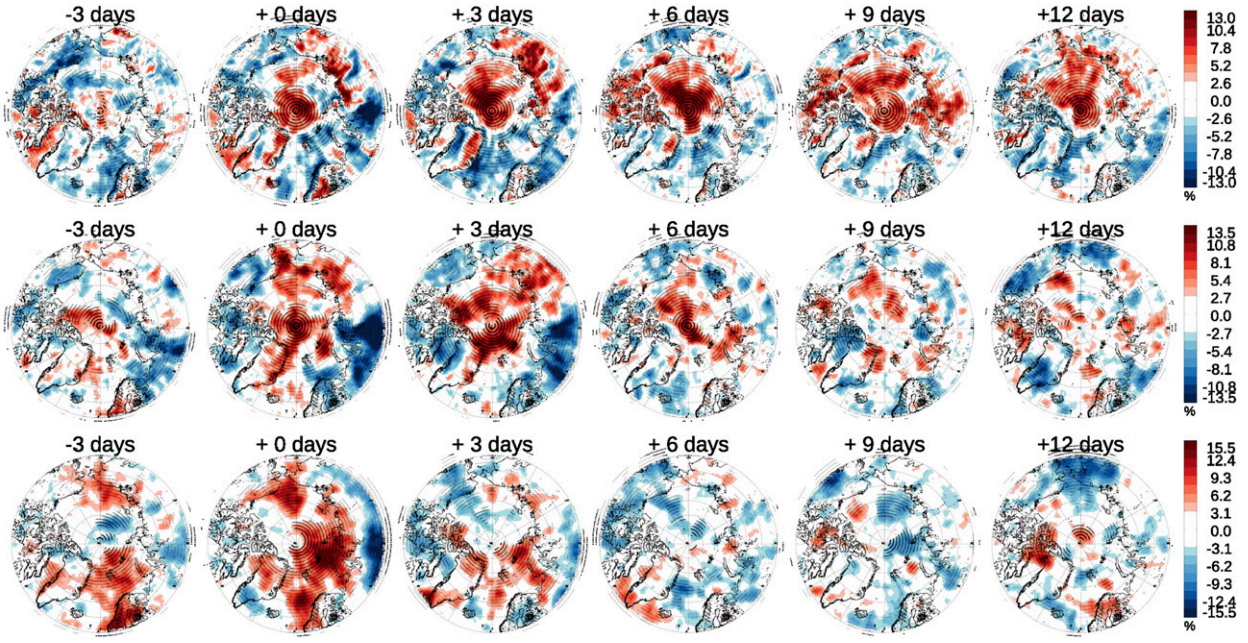

FIG. 10. Composites of the time evolution of anomalies in (top) low-, (middle) middle-, and (bottom) high-level cloud during downward IR events. Composite values with significance levels higher than 90% are labeled with a black plus sign.

14. It appears that the IR events generate more high-level cloud, relatively less middle-level cloud, and even less low-level cloud anomalies in their early stages until lag day 5. It should be noted that the mean cloud amount over the GIN Seas is climatologically high (Liu et al. 2012a) and thus low-level cloud may not become much higher even with greater moisture. The correlation of average anomalies between high-level cloud amount and moisture convergence is over 0.90 at 95% significance level, whereas it is quite small and not significant with middle-level and low-level cloud amount. In the late stages of the IR events, more low-level cloud anomalies appear than middle- and high-level cloud. This low-level cloud positive anomaly at the late stage might be due to more evaporation through the open water because of the sea ice melting from the stronger all-sky DLR besides the impact of moisture intrusions.

The strong tropospheric stability over the Arctic Ocean starts to weaken from lag day 0. The negative anomalies appear first over the Kara Sea at lag day 0 and then extend to the whole Arctic Ocean at lag day 9 and afterward (Fig. 11). Averaged anomalies over the area between 70° and 90°N are larger than 0.5 standard deviation after lag day 5 and remain steady until lag day 14 (Fig. 6b). It should be noted that the overall lower troposphere is very stable despite the negative stability anomalies as shown in Fig. 11. This stable condition may help maintain the positive low-level cloud anomalies over the central Arctic Ocean. Schweiger et al. (2008) associate a decrease in static stability with less low-level cloud and more middle-level cloud. The changes in the lower tropospheric stability may be related to the maintenance of the anomalously large middle-level cloud amount anomalies after lag day 3 as shown in Fig. 10.

4) CLOUD CHANGES IN SATELLITE DATASETS

Evolution of total cloud amount anomalies from MODIS over the period 2000–16 in the Arctic during the IR events shows similar features as those from ERA-Interim total cloud amount anomalies from 1990 to 2016 and from 2000 to 2016 (Fig. S12). In general, all anomalies are positive over most of the Arctic Ocean, the Canada Archipelago Seas, and northeastern Russia, and negative over land. All the positive anomalies appear from lag day 0 and can last until lag day 12.

The absolute magnitude of the anomalies from MODIS is larger than those from ERA-Interim. It should be noted that the MODIS cloud amount standard deviation, approximately 9.0%, is higher than that of ERA-Interim total cloud, which is 4.6%. The standard deviation difference can be attributed to the different approaches to determining total cloud amount from MODIS and ERA-Interim, and to the length of MODIS data and ERA-Interim data in this study, 17 and 27 years respectively. It appears that positive MODIS cloud amount anomalies appear over a larger area than for ERA-Interim, although the area may become more similar to that of ERA-Interim with the consideration of its larger

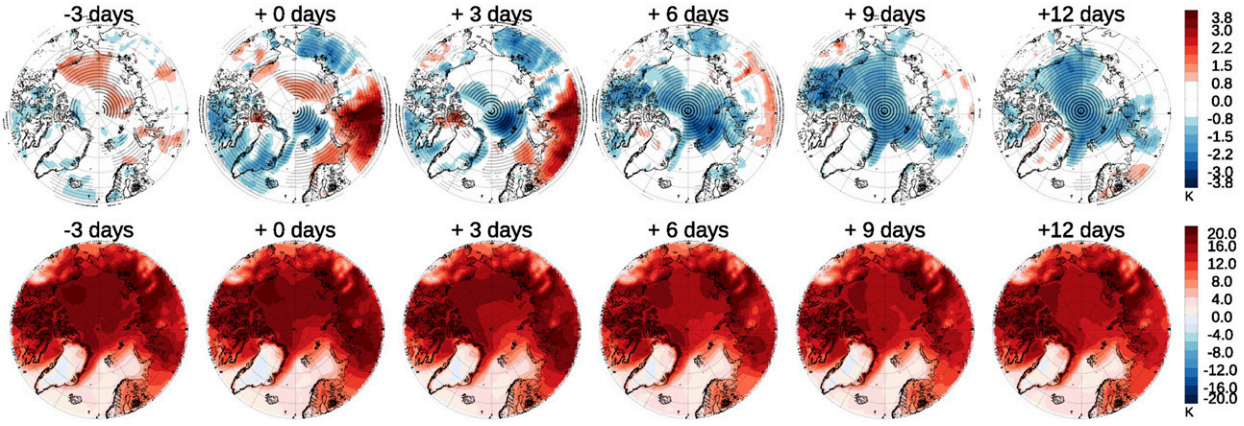

FIG. 11. Composites of the time evolution of atmosphere stability (top) anomalies and (bottom) the mean during downward IR events. Atmospheric stability is the potential temperature difference between 850 hPa and the surface. Composite values with a significance level higher than 90% are labeled with a black plus sign.

standard deviation. For the averaged anomalies over the area between 70° and 90°N normalized by standard deviation, MODIS total cloud amount anomalies follow the ERA-Interim total cloud amount anomalies closely when 9.0% standard deviation is applied (Fig. S13). This shows that ERA-Interim reasonably simulates the mean total cloud amount anomalies over the Arctic Ocean.

Cloud amount determined from satellite imagers has large uncertainties due to the challenging conditions in the Arctic, especially in the wintertime (Liu et al. 2004, 2010). Satellite-borne active sensors provide better estimates of cloud amount and microphysical properties (Liu et al. 2012a, 2017). Because of the limited sample numbers of the observations from active sensors, like *CloudSat*, only the composite anomalies averaged over the Arctic Ocean are calculated and shown, rather than their spatial distributions. Cloud amount anomalies averaged over the Arctic Ocean are positive for total cloud and for high-, middle-, and low-level clouds from lag day −2 to lag day 5 and are also greater than those from ERA-Interim (Fig. S14). This verifies the moisture intrusion impact on the cloud amount changes from ERA-Interim and may also suggest that ERA-Interim underestimates the impact of the IR events on the positive cloud amount anomalies. The cloud amounts become normal after lag day 5, whereas the anomalies from ERA-Interim remain positive after lag day 10. This difference may come from the different areas that the cloud amount anomalies are averaged, with an area between 70° and 90°N for ERA-Interim and an area mainly between 78° and 81°N for *CloudSat* (Fig. 3 in Liu 2015). Standardized cloud ice water content anomalies from the 2B-CWC-RO averaged over the Arctic Ocean also show similar trends as that of ERA-Interim, with positive anomalies from lag day −3 to lag day 4 (Fig. S15). After lag day 4, the anomalies from 2B-CWC-RO become unstable, partly due to the limited number of samples. The similarity of both trends helps to verify that IR events can lead to a cloud ice water content increase. The agreement in the cloud amount and cloud ice water content anomalies during IR events between ERA-Interim and MODIS, 2B-GEOPROF, and 2B-CWC-RO provides support for the findings in previous sections based on ERA-Interim.

4. Summary and conclusions

We studied the response of cloud, DLR, and other variables to the moisture intrusions into the Arctic during winter, from November to March. Two definitions related to Arctic moisture intrusions are explored, one following the definitions of Arctic moisture intrusions by Woods et al. (2013) and Johansson et al. (2017) and the other following the definition of a downward IR event by Park et al. (2015). These two definitions are related, in that IR events are typically preceded by an Arctic moisture intrusion 3 days earlier from one of the four geographic sectors: the Atlantic, Barents/Kara Sea, Pacific, and Labrador Sea. The primary conclusions of this study are as follows:

- Forty-eight of the 50 downward IR events are preceded by moisture intrusions; 41 of the 50 downward IR events are preceded by moisture intrusions from the Atlantic side of the Arctic Ocean (i.e., the Atlantic and Barents/Kara sectors); 2 of the 50 events are not preceded by moisture intrusions. Not all moisture intrusions lead to an IR event.
- For a moisture intrusion that develops into a downward IR event, a time-evolving large-scale circulation

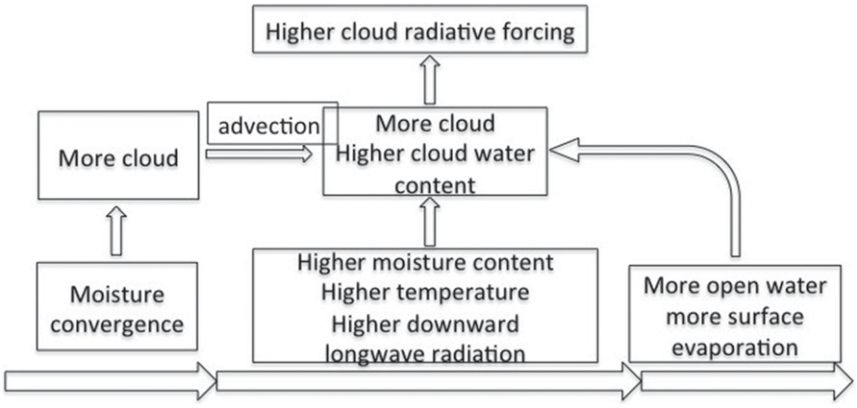

FIG. 12. Schematic figure of the cloud response to moisture intrusions.

pattern favors the moisture and heat flux from the Atlantic Ocean into that side of the Arctic, farther into the central Arctic, and then to the Pacific side of the Arctic Ocean.

- Composite analysis of Arctic moisture intrusions shows greater all-sky DLR, clear-sky DLR, and longwave CRF from lag day 0 to after lag day 9. The greater clear-sky DLR is attributed to higher temperature and total column water vapor, while the greater longwave CRF comes from higher cloud amount and cloud water content. Anomalies during the moisture intrusions in the Atlantic and Barents/Kara sectors are limited to the Atlantic side of the Arctic Ocean; anomalies during the moisture intrusions in the Pacific sector are limited to the Pacific side of the Arctic Ocean; anomalies during the moisture intrusions in the Labrador sector are limited to the area from Greenland to the Canada Archipelago Seas. The anomalies averaged over the whole Arctic Ocean are much smaller. Geopotential height anomalies during the moisture intrusions in each sector favor the moisture/heat advection into the Arctic, and this large-scale atmospheric pattern anomaly remains largely unchanged during the event with varying magnitude.
- Composite analysis of downward IR events shows that moisture intrusions can lead to greater basinwide all-sky DLR, clear-sky DLR, and longwave CRF for a long period of time. Anomalously high clear-sky DLR shows a similar time evolution to those of all-sky DLR anomalies. This positive anomaly can be attributed to higher air temperature at every layer and higher total column water vapor. Anomalously greater longwave CRF also shows a similar time evolution to those of all-sky and clear-sky DLR anomalies. This positive anomaly can be attributed to greater cloud amount, cloud ice water content, and cloud liquid water content. The CRF anomaly accounts for approximately 40% of the all-sky anomalies.
- During the moisture intrusions and downward IR events, positive high- and middle-level cloud anomalies appear in the early stage, and more low-level cloud anomalies appear in the late stage. The total cloud amount anomalies are dominated by the anomalies in the low-level cloud.

Clouds may respond to the moisture intrusions in three ways (Fig. 12), as follows. 1) A strong pulse at the beginning of the moisture intrusion events is followed by a quick dissipation in the moisture convergence, and its evolution is well correlated with the high-level cloud amount anomalies and also in middle-level cloud. These positive cloud amount anomalies in high-level and middle-level clouds over the Nansen Basin and the Kara Sea can be advected to the central Arctic Ocean and may persist because of the stable atmospheric conditions in the Arctic (Liu et al. 2007). 2) During moisture intrusions, clouds appear in the advected warmer and moister air mass because of radiative cooling to space and diffusive cooling to the surface; the cloud remains as a result of the lack of cloud dissipation mechanisms (Herman and Goody 1976; Klein and Hartmann 1993; Curry et al. 1996). Also, in an anticyclonic pattern as often occurs in Arctic winter, the moisture advected in the upper layers through the large-scale circulation can be transported downward to maintain the low-level cloud, as suggested by Curry (1983) and Khrgian (1977). 3) More evaporation from the open water caused by sea ice melting because of higher DLR (Park et al. 2015) can also contribute to the greater low-level cloud amount in the late stage of the moisture intrusions (Kay and Gettelman 2009; Palm et al. 2010; Liu et al. 2012b; Chernokulsky et al. 2017). It should be noted that the temperature, total column water vapor, and cloud ice

water content all have larger than one standard deviation anomalies from lag day 0 to lag day 5 or beyond, while the anomalies of the total and the low-, middle-, and high-level cloud amount do not exceed one standard deviation.

Analysis-based satellite cloud products are consistent with those from ERA-Interim. The spatial patterns of MODIS total cloud amount anomalies are similar to those from ERA-Interim during the moisture intrusions, and normalized basinwide mean total cloud amount anomalies from MODIS resemble those from ERA-Interim. Composite analysis from *CloudSat* 2B-GEOPROF and 2B-CWC-RO show similar time evolutions of cloud amount and cloud ice water content averaged over the Arctic Ocean with those from ERA-Interim. The agreement between ERA-Interim and satellite products provides supports for the findings based on ERA-Interim.

This study focused on the composite response of cloud, DLR, and other variables during the moisture intrusions into the Arctic during winter. The frequency of moisture intrusions has been increasing in December and January (Woods and Caballero 2016). How this trend affects the response needs further investigation. This study uses ERA-Interim as the main dataset, with total cloud amount from MODIS and cloud amount and ice water content from *CloudSat*. With long-term satellite datasets available for temperature and moisture profiles, surface radiation flux, cloud amount, and cloud properties in the Arctic, this topic is worth further investigation. Analysis in other seasons would involve both longwave radiation and solar radiation and needs further investigation.

Acknowledgments. Yinghui Liu would like to thank Dr. Jonathan Martin and Dr. Tristan L'Ecuyer for their comments and discussion at the early stage of this work. Yinghui Liu was supported by projects from the NOAA Climate Data Records program and the Joint Polar Satellite System (JPSS) Program Office (NA15NES4320001). Steve Vavrus was supported by National Science Foundation Office of Polar Programs PLR-1304398 and NOAA Climate Program Office under Climate Variability and Predictability Program NA15OAR4310166. Cian Woods would like to acknowledge the support of Vetenskapsrådet under Contract E0531901. MODIS data were obtained from the Atmosphere Archive and Distribution System of the NASA Goddard Space Flight Center, at https://ladsweb.nascom.nasa.gov/. The ERA-Interim data were provided by the European Centre for Medium-Range Weather Forecasts (ECMWF) from http://apps.ecmwf.int/datasets/. *CloudSat* Standard Data Products are distributed by the *CloudSat* Data Processing Center, located at the Cooperative Institute for Research in the Atmosphere at Colorado State University in Fort Collins. The views, opinions, and findings contained in this report are those of the author(s) and should not be construed as an official National Oceanic and Atmospheric Administration or U.S. Government position, policy, or decision.

REFERENCES

Ackerman, S., K. Strabala, W. Menzel, R. Frey, C. Moeller, and L. Gumley, 1998: Discriminating clear sky from clouds with MODIS. *J. Geophys. Res.*, **103**, 32 141–32 157, https://doi.org/10.1029/1998JD200032.

Alexeev, V. A., J. E. Walsh, V. V. Ivanov, V. A. Semenov, and A. V. Smirnov, 2017: Warming in the Nordic Seas, North Atlantic storms and thinning Arctic sea ice. *Environ. Res. Lett.*, **12**, 084011, https://doi.org/10.1088/1748-9326/aa7a1d.

Austin, R. T., A. J. Heymsfield, and G. L. Stephens, 2009: Retrieval of ice cloud microphysical parameters using the CloudSat millimeter-wave radar and temperature. *J. Geophys. Res.*, **114**, D00A23, https://doi.org/10.1029/2008JD010049.

Chernokulsky, A. V., I. Esau, O. N. Bulygina, R. Davy, I. I. Mokhov, S. Outten, and V. A. Semenov, 2017: Climatology and interannual variability of cloudiness in the Atlantic Arctic from surface observations since the late nineteenth century. *J. Climate*, **30**, 2103–2120, https://doi.org/10.1175/JCLI-D-16-0329.1.

Curry, J. A., 1983: On the formation of continental polar air. *J. Atmos. Sci.*, **40**, 2278–2292, https://doi.org/10.1175/1520-0469(1983)040<2278:OTFOCP>2.0.CO;2.

——, W. B. Rossow, D. Randall, and J. L. Schramm, 1996: Overview of Arctic cloud and radiation characteristics. *J. Climate*, **9**, 1731–1764, https://doi.org/10.1175/1520-0442(1996)009<1731:OOACAR>2.0.CO;2.

Dee, D. P., and Coauthors, 2011: The ERA-Interim reanalysis: Configuration and performance of the data assimilation system. *Quart. J. Roy. Meteor. Soc.*, **137**, 553–597, https://doi.org/10.1002/qj.828.

Frey, R., S. Ackerman, Y. Liu, K. Strabala, H. Zhang, J. Key, and X. Wang, 2008: Cloud detection with MODIS. Part I: Improvements in the MODIS cloud mask for Collection 5. *J. Atmos. Oceanic Technol.*, **25**, 1057–1072, https://doi.org/10.1175/2008JTECHA1052.1.

Herman, G., and R. Goody, 1976: Formation and persistence of summertime Arctic stratus clouds. *J. Atmos. Sci.*, **33**, 1537–1553, https://doi.org/10.1175/1520-0469(1976)033<1537:FAPOSA>2.0.CO;2.

Johansson, E., A. Devasthale, M. Tjernström, A. M. L. Ekman, and T. L'Ecuyer, 2017: Response of the lower troposphere to moisture intrusions into the Arctic. *Geophys. Res. Lett.*, **44**, 2527–2536, https://doi.org/10.1002/2017GL072687.

Kay, J. E., and A. Gettelman, 2009: Cloud influence on and response to seasonal Arctic sea ice loss. *J. Geophys. Res.*, **114**, D18204, https://doi.org/10.1029/2009JD011773.

Khrgian, A. K. H., 1977: Structure of stratiform clouds. 1. *Izv. Acad. Sci. USSR Atmos. Oceanic Phys.*, **13**, 792–797.

Klein, S. A., and D. L. Hartmann, 1993: The seasonal cycle of low stratiform clouds. *J. Climate*, **6**, 1587–1606, https://doi.org/10.1175/1520-0442(1993)006<1587:TSCOLS>2.0.CO;2.

Letterly, A., J. Key, and Y. Liu, 2016: The influence of winter cloud on summer sea ice in the Arctic, 1983–2013. *J. Geophys. Res. Atmos.*, **121**, 2178–2187, https://doi.org/10.1002/2015JD024316.

Liu, Y., 2015: Estimating errors in cloud amount and cloud optical thickness due to limited spatial sampling using a satellite imager as a proxy for nadir-view sensors. *J. Geophys. Res. Atmos.*, **120**, 6980–6991, https//doi.org/10.1002/2015JD023507.

——, and J. R. Key, 2014: Less winter cloud aids summer 2013 Arctic sea ice return from 2012 minimum. *Environ. Res. Lett.*, **9**, 044002, https://doi.org/10.1088/1748-9326/9/4/044002.

——, and ——, 2016: Assessment of Arctic cloud cover anomalies in atmospheric reanalysis products using satellite data. *J. Climate*, **29**, 6065–6083, https://doi.org/10.1175/JCLI-D-15-0861.1.

——, ——, R. A. Frey, S. A. Ackerman, and W. P. Menzel, 2004: Nighttime polar cloud detection with MODIS. *Remote Sens. Environ.*, **92**, 181–194, https://doi.org/10.1016/j.rse.2004.06.004.

——, ——, J. Francis, and X. Wang, 2007: Possible causes of decreasing cloud cover in the Arctic winter, 1982–2000. *Geophys. Res. Lett.*, **34**, L14705, https://doi.org/10.1029/2007GL030042.

——, S. A. Ackerman, B. C. Maddux, J. R. Key, and R. A. Frey, 2010: Errors in cloud detection over the Arctic using a satellite imager and implications for observing feedback mechanisms. *J. Climate*, **23**, 1894–1907, https://doi.org/10.1175/2009JCLI3386.1.

——, J. R. Key, S. A. Ackerman, G. G. Mace, and Q. Zhang, 2012a: Arctic cloud macrophysical characteristics from CloudSat and CALIPSO. *Remote Sens. Environ.*, **124**, 159–173, https://doi.org/10.1016/j.rse.2012.05.006.

——, ——, Z. Liu, X. Wang, and S. Vavrus, 2012b: A cloudier Arctic expected with diminishing sea ice. *Geophys. Res. Lett.*, **39**, L05705, https://doi.org/10.1029/2012GL051251.

——, M. D. Shupe, Z. Wang, and G. Mace, 2017: Cloud vertical distribution from combined surface and space radar–lidar observations at two Arctic atmospheric observatories. *Atmos. Chem. Phys.*, **17**, 5973–5989, https://doi.org/10.5194/acp-17-5973-2017.

Liu, Z., and A. Schweiger, 2017: Synoptic conditions, clouds, and sea ice melt onset in the Beaufort and Chukchi seasonal ice zone. *J. Climate*, **30**, 6999–7016, https://doi.org/10.1175/JCLI-D-16-0887.1.

Mace, G. G., Q. Zhang, M. Vaughan, R. Marchand, G. Stephens, C. Trepte, and D. Winker, 2009: A description of hydrometeor layer occurrence statistics derived from the first year of merged Cloudsat and CALIPSO data. *J. Geophys. Res.*, **114**, D00A26, https://doi.org/10.1029/2007JD009755.

Marchand, R., G. G. Mace, T. Ackerman, and G. Stephens, 2008: Hydrometeor detection using *Cloudsat*—An Earth-orbiting 94-GHz cloud radar. *J. Atmos. Oceanic Technol.*, **25**, 519–533, https://doi.org/10.1175/2007JTECHA1006.1.

Palm, S. P., S. T. Strey, J. Spinhirne, and T. Markus, 2010: Influence of Arctic sea ice extent on polar cloud fraction and vertical structure and implications for regional climate. *J. Geophys. Res.*, **115**, D21209, https://doi.org/10.1029/2010JD013900.

Park, H.-S., S. Lee, S.-W. Son, S. B. Feldstein, and Y. Kosaka, 2015: The impact of poleward moisture and sensible heat flux on Arctic winter sea ice variability. *J. Climate*, **28**, 5030–5040, https://doi.org/10.1175/JCLI-D-15-0074.1.

Schweiger, A. J., R. W. Lindsay, S. Vavrus, and J. A. Francis, 2008: Relationships between Arctic sea ice and clouds during autumn. *J. Climate*, **21**, 4799–4810, https://doi.org/10.1175/2008JCLI2156.1.

Stephens, G. L., and Coauthors, 2002: The CloudSat mission and the A-Train: A new dimension of space-based observations of clouds and precipitation. *Bull. Amer. Meteor. Soc.*, **83**, 1771–1790, https://doi.org/10.1175/BAMS-83-12-1771.

Walsh, J. E., W. L. Chapman, and D. H. Portis, 2009: Arctic cloud fraction and radiative fluxes in atmospheric reanalyses. *J. Climate*, **22**, 2316–2334, https://doi.org/10.1175/2008JCLI2213.1.

Woods, C., and R. Caballero, 2016: The role of moist intrusions in winter Arctic warming and sea ice decline. *J. Climate*, **29**, 4473–4485, https://doi.org/10.1175/JCLI-D-15-0773.1.

——, ——, and G. Svensson, 2013: Large-scale circulation associated with moisture intrusions into the Arctic during winter. *Geophys. Res. Lett.*, **40**, 4717–4721, https://doi.org/10.1002/grl.50912.

Zib, B. J., X. Dong, B. Xi, and A. Kennedy, 2012: Evaluation and intercomparison of cloud fraction and radiative fluxes in recent reanalyses over the Arctic using BSRN surface observations. *J. Climate*, **25**, 2291–2305, https://doi.org/10.1175/JCLI-D-11-00147.1.

Zygmuntowska, M., T. Mauritsen, J. Quaas, and L. Kaleschke, 2012: Arctic Clouds and Surface Radiation—A critical comparison of satellite retrievals and the ERA-Interim reanalysis. *Atmos. Chem. Phys.*, **12**, 6667–6677, https://doi.org/10.5194/acp-12-6667-2012.